Biophysical Journal, Volume *117*

Supplemental Information

Effect of Post-Translational Modifications and Mutations on Amyloid-β Fibrils Dynamics at N Terminus

Liliya Vugmeyster, Dan F. Au, Dmitry Ostrovsky, Brian Kierl, Riqiang Fu, Zhi-wen Hu, and Wei Qiang

Supplementary Material **Effect of Post-translational Modifications and Mutations on Amyloid-β fibrils Dynamics at N-terminus**

Liliya Vugmeyster,[1,]* Dan F. Au,[1] Dmitry Ostrovsky,[2] Brian Kierl,[1] Riqiang Fu,[3] Zhi-wen Hu, [4] Wei Qiang[4]

[1] Department of Chemistry, University of Colorado Denver, Denver CO USA 80204

[2] Department of Mathematics, University of Colorado Denver, Denver CO USA 80204

[3] National High Field Magnetic Laboratory, Tallahassee, FL USA 32310

[4]Department of Chemistry, Binghamton University, Binghamton, New York USA 13902

*To whom correspondence should be addressed: Liliya Vugmeyster, 1201 Laurimer Street, Denver CO 80204, USA email: LILIYA.VUGMEYSTER@UCDENVER.EDU

Supporting file S1. Details of Experimental and Modeling Procedures

I. Peptide synthesis

The $A\beta_{1-40}$ peptides were prepared by using solid-state peptide synthesis (performed by Thermofisher Scientific Co, Rockford, IL). Fluorenylmethyloxycarbonyl (FMOC)-Phenylalanine-ring-d_5 and FMOC-Glycine-C_α-d_2, were purchased from Cambridge Isotopes Laboratories (Andover, MA). The native sequence is DAEFRHDSGYEVHHQKLVFFAEDVGSNKGAIIGLMVGGVV. The following modifications were introduced for the variants: truncation of the first two residues (ΔE3), D7-isoD7 (isoD7), phosphorylation of serine-8 (pS8), E22 deletion mutant (E22Δ), D23 to N substitution (D23N). The peptides were purified by reversed-phase HPLC and their identity and purity were confirmed by mass spectrometry and reversed-phase HPLC.

II. Preparation of fibril samples

The pS8 and ΔE3: fibrils were grown following the generation seeding protocols: To produce parent fibrils (G0), lyophilized peptides were dissolved in hexafluoroisoproponal (HFIP) to 2.0 mg/mL and incubated overnight at ambient temperature. The HFIP was removed by N_2 flow and followed high-vacuum for at least 3 hours. The resultingpeptide film was dissolved in dimethyl sulfoxide (DMSO) to 2.0 mM, sonicated on ice-bath for 3 minutes, centrifuged at 14,000 rpm for 10 minutes to remove any preformed aggregates, and diluted with 10 mM monosodium phosphate buffer (pH 7.4, 0.05% NaN_3) to the final concentration of 0.5 mg/mL. The solution was incubated at 37 ºC with 200 rpm orbital agitation for 72 hours. To obtain the first-generation seeded fibrils (G1), G0 fibrils were sonicated on ice-bath with a probe sonicator for 30-60 seconds (continuous power output, 20% duty cycle). G1 generation was prepared by dissolving the lyophilized peptide in DMSO followed by immediate addition to the phosphate buffer containing G0 seeds in 1:10 molar ratio, with a final peptide concentration of 0.5 mg/mL. G1 fibrils growth was achieved by incubation with gentle 40 rpm orbital agitation for 24 hours at room temperature. The following generations were prepared using the same protocol as for G1, and the last-generation fibrils (G6 for pS8 and G5 for ΔE3) were used as seeds for the NMR bulk samples.

IsoD7 cross-seeded with wild-type $A\beta_{1-40}$: the seeds consisted of the wild-type $A\beta_{1-40}$ fibrils in the 3-fold symmetric polymorph in the phosphate buffer at 0.5 mg/mL concentration. Lyophilized isoD7 $A\beta_{1-40}$ peptide was solubilized in DMSO to 5.0 mM. The seeds were sonicated for 1.5 min using a probe sonicator. A 1:10 molar ratio of the wild-type $A\beta_{1-40}$ seeds to the isoD7. $A\beta_{1-40}$ solubilized peptide was combined in the phosphate buffer to yield a total protein concentration of 0.4 mg/mL and immediately filtered through a 0.22 μm filter. The solution was incubated for 3-5 days with gentle 40 rpm orbital agitation at room temperature.

E22Δ: Lyophilized peptides were dissolved at a 5 mM concentration in DMSO and immediately transferred to the phosphate buffer to the final concentration of 0.3 mg/mL. The fibrils were allowed to grow for at least 4 days at room temperature at quiescent conditions. TEM images were taken immediately upon dissolving in the buffer, at 2-3 hours and at 24-30 hours after dissolution.

Collection and hydration of bulk samples for NMR analysis: The bulk fibrils were pelleted by centrifuging at 300,000 *g* for 7-9 hours. The exceptions were Zn^{2+}-induced aggregates and ΔE3 fibrils, for which the fibrils were collected by centrifugal dialysis using Amicon filters with 3 kDa molecular weight cut-off. Collected fibrils were re-suspended in deionized water, rapidly frozen with liquid nitrogen, and lyophilized. A hydrated state with a water content of 200% by weight was achieved by pipetting deuterium-depleted H_2O. The samples were packed in 5 mm NMR tubes (cut to 21 mm length) using Teflon tape to center the sample volume in the coil of the NMR probe.

III. Negatively-stained transmission electron microscopy

Samples were stored at room temperature and diluted to about 0.1 mg/mL with hydro, millipore-filtered water. Samples were negatively stained by using the drop method (*1*) in the following manner. Four microliter aliquots of the sample, millipore-filtered water, and 2% uranyl acetate aqueous stain were applied sequentially to a freshly glow-discharged,(*2*) Formvar carbon-coated 300 mesh copper grid for the following incubation times: 2 min, 10 sec, and 2 min, respectively. Each 4 μl droplet was removed by wicking with filter paper for 5 sec. The filter paper was blotted prior to the addition of the next droplet. After staining, the grid was air-dried under a vacuum for 20 min. Images were collected under low dose conditions of 120,000× using the FEI Tecnai G2 Spirit Biotwin microscope operating at 80 kV.

IV. NMR spectroscopy

Experiments were performed using 9.4 T (University of Colorado at Denver) and 14.1 T (National High Magnetic Field Laboratory) spectrometers equipped with the Bruker neo consoles and static probes with 5 mm diameter coils: the wide-line low-E probe(*3*) for the 14.1 T spectrometer and the Phoenix probe for the 9.6 T spectrometer.

Line shape experiments were performed with a quadrupole echo pulse sequence based on an eight-step phase cycle(*4*), with a delay of 31-36 μs between 90° pulses. A line broadening function of 0.5 to 2 kHz was employed to enhance the signal.

The $R_{1\rho}$ experiments were performed at 9.4 T and 37°C using the methodology described in previous work(*5*) with the pulse sequence of Figure S1. Spin-lock times varied between 200 μs and 15 ms (a total of 12 relaxation delays) and powers ranged between 5 and 20 kHz. The upper limit was determined by the sensitivity of the sample to heating. The number of scans varied between 2048 and 8000 depending on each sample's sensitivity.

^2H QCPMG time-domain measurements (*6*) were performed at 14.1 T field strength and 37°C. The pulse sequence used for the time domain acquisition(*7*) and further experimental details are shown in Figure S1. The multiple echo acquisition scheme employed echo times between 53 and 363 μs with the rf irradiation frequency set exactly on resonance. The lower limit of the pulse spacing was determined by system electronic/acoustical ringing, while the upper limit was determined by sensitivity factors. The number of scans varied between 4096 and 81920 depending on the signal-to-noise ratio in each sample. The inter-scan delay was set to 0.2-0.4 sec and 32 dummy scans were utilized.

V. Motional modeling and fitting of the data

Motional modeling followed the protocols described previously.(*5, 7, 8*) Below we present an overview of the procedures.

Theory overview

Density matrix for the spin-1 system can be written in the basis of the following operators(*9*)

$$\hat{S}_x = \frac{1}{2}\begin{pmatrix} 0 & 1 & 0 \\ 1 & 0 & 1 \\ 0 & 1 & 0 \end{pmatrix}, \hat{S}_y = \frac{1}{2}\begin{pmatrix} 0 & -i & 0 \\ i & 0 & -i \\ 0 & i & 0 \end{pmatrix}, \hat{J}_x = \frac{1}{2}\begin{pmatrix} 0 & -i & 0 \\ i & 0 & i \\ 0 & -i & 0 \end{pmatrix}, \hat{J}_y = \frac{1}{2}\begin{pmatrix} 0 & 1 & 0 \\ 1 & 0 & -1 \\ 0 & -1 & 0 \end{pmatrix} \quad \text{(S-1)}$$

$$\hat{S}_z = \frac{1}{\sqrt{2}}\begin{pmatrix} 1 & 0 & 0 \\ 0 & 0 & 0 \\ 0 & 0 & -1 \end{pmatrix}, \hat{J}_z = \frac{1}{\sqrt{2}}\begin{pmatrix} 0 & 0 & -i \\ 0 & 0 & 0 \\ i & 0 & 0 \end{pmatrix}, \hat{Q} = \frac{1}{\sqrt{6}}\begin{pmatrix} 1 & 0 & 0 \\ 0 & -2 & 0 \\ 0 & 0 & 1 \end{pmatrix}, \hat{K} = \frac{1}{\sqrt{2}}\begin{pmatrix} 0 & 0 & 1 \\ 0 & 0 & 0 \\ 1 & 0 & 0 \end{pmatrix}$$

They obey the following normalization condition $\mathrm{tr}(O_k^{+}O_l) = \delta_{kl}$.

During the saturation period and in the frame rotating with the Larmor frequency the secular part of the Hamiltonian is given by:

$$\hat{H}_{sec} = \sqrt{\frac{2}{3}}\omega_Q \hat{Q} + \sqrt{2}\omega_{RF}\hat{S}_x,$$

where ω_{RF} is the RF field strength.

$$\omega_Q = \frac{3\pi}{2} C_q \left(\frac{3\cos^2\theta - 1}{2} + \frac{\eta}{2}\sin^2\theta\cos 2\phi\right) \quad \text{(S-2)}$$

is the frequency of the secular part of quadrupole interaction with angles (θ, ϕ) representing the rotation of the principal-axis system (PAS) of the quadrupole interaction with respect to the laboratory frame. The quadrupolar coupling constant is given by $C_q = \frac{e^2 qQ}{h}$, and $\eta \equiv \frac{q_{xx} - q_{yy}}{q_{zz}}$ represents the asymmetry of the tensor, defined in the interval $0 \le \eta \le 1$ with $|q_{zz}| \ge |q_{yy}| \ge |q_{xx}|$. eQ is the electric quadrupole moment of the nucleus and eq is the largest component of the electric field gradient.

In the presence of molecular motions, the value of ω_Q for an individual crystallite does not remain constant, but changes due to changes in the PAS orientation. In addition to the dependence of ω_Q originating from molecular motions, in solids powder there is an additional dependence of ω_Q on the orientation of the crystallite to the static magnetic field, as it the case for all anisotropic interactions.
Additional terms in the Hamiltonian include quadrupole interaction terms fluctuating with the single and double Larmor frequencies. They are of less significance in these measurements then relaxation due to fluctuations in the value of ω_Q and are treated separately through the Redfield theory.(*10*)

The evolution of the density matrix can be written using the basis of Eq.(S-1) in the superoperator formalism. Liouville - von Neumann formalism combines the Hamiltonian super-operator for the spin density matrix with Markovian jumps between states with different values of ω_Q simulating various spin environments. It, therefore, includes the relaxation due to the fluctuations in the ω_Q value, which, in general, cannot be treated within the Redfield approximation and the full Liouvillian treatment becomes necessary.(*11*)

If intramolecular motions are given by discrete jumps between *n* sites with different values of ω_Q sampled by the conformational exchange, the evolution matrix becomes

$$\frac{d}{dt}\begin{pmatrix}\rho_1\\ \rho_2\\ \vdots\\ \rho_n\end{pmatrix}=\begin{pmatrix}A_1+K_{11} & K_{12} & \cdots & K_{1n}\\ K_{21} & A_2+K_{22} & \cdots & K_{2n}\\ \vdots & \vdots & \ddots & \vdots\\ K_{n1} & K_{n2} & \cdots & A_n+K_{nn}\end{pmatrix}\begin{pmatrix}\rho_1\\ \rho_2\\ \vdots\\ \rho_n\end{pmatrix} \quad \text{(S-3)}$$

where $\rho_i = (S_x, J_x, K, Q)^T$ are the components of the density matrix for the site *i* in the basis of the operators of Eq.(1) with coefficients corresponding to the components of the density matrix as for the operators themselves, but without hats. The other 4 components of the density matrix are decoupled under both the on-resonance $R_{1\rho}$ and QCPMG conditions used in the experiment.

The 4×4 evolution A_i matrices which include coherent evolution given by $\widehat{H}_{sec}$ are given by:

$$A=\begin{pmatrix}0 & -\omega_q & 0 & 0\\ \omega_q & 0 & -\omega_{sl} & -\sqrt{3}\omega_{sl}\\ 0 & \omega_{sl} & 0 & 0\\ 0 & \sqrt{3}\omega_{sl} & 0 & 0\end{pmatrix} \quad \text{(S-4)}$$

The off-diagonal blocks in Eq.(S-3) represent conformational exchange and are given by $K_{ij} = k_{ij}I$, where *I* is the 4×4 identity matrix and the diagonal blocks $K_{ii} = -\sum_{j\neq i} K_{ji}$ provide conservation of probability.

The exchange matrix K_{ij} combines components responsible for the isotropic diffusion and the conformational exchange between the free diffusion state and the bound state, according to the following scheme:

$$K=\left(\begin{array}{c|c}\text{diffusion} & \begin{array}{c}\text{exchange}\\ \text{with bound}\\ \text{state}\end{array}\\ \hline \text{exchange with bound state} & \end{array}\right)$$

The block of the exchange matrix K_{ij} responsible for the diffusion, is represented by nearest neighbor jumps with sites of equal populations distributed (almost) uniformly on the surface of the sphere and with identical exchange rates between the sites, $K_{ij} = k_D$. We used the program DistMesh,(*12*) which creates the uniform distribution of sites by assuming a linear repulsive force and solving for the equilibrium. The inclusion of $N_D = 192$ sites is sufficient to adequately represent the isotropic diffusion process and this leads to the following range of jump angles in the crystal-fixed frame between the sites: 13.7–18.7°. Due to the spin 1 symmetry properties, only the second-order spatial spherical harmonics give rise to the spectral densities. Thus, the second-order eigenfunction of the Smoluchowski diffusion equation encodes the spatial reorientation and the corresponding eigenvalue is related to the diffusion coefficient *D* as $Dl(l+1) = 6D$. As expected, the simulated eignevalues of K_{ij} appear in groups of $2l+1$, corresponding to the eignevectors with the angular momentum *l* of the continuous limit of the diffusion equation. The five eigenvalues λ_2 corresponding to $l = 2$ are then averaged to obtain the numerical value of *D*. This establishes the correspondence between *D* and k_D as $k_D = 6D/\langle\lambda_2\rangle$.

To include the exchange process, one additional site with a fixed angular position corresponding to the bound state was added to yield a total of $N_D + 1$ sites. The exchange was modeled by jumps between every site describing the spherical diffusion and the bound-state site with an arbitrary fixed angular position with

the rate k_{ex}/N_D. Modeled in this fashion, the relative tensor orientation in the free and bound states is averaged over the uniform spherical distribution.

Computational modeling details

Each of the two exchange process was modeled by jumps between every site describing the spherical diffusion and the bound-state site. The relative weights of each site were expressed through the ratio of the forward and reverse rate constants for the exchange process. Modeling the exchange with two free states and one bound state included two sets of 192 sites describing the surface of two spheres with the corresponding nearest-neighbor jump constants within each set, as well as independent exchange constants between every site of each of the two sets and an arbitrarily fixed site in the crystal-fixed frame, corresponding to the bound state. The direct exchange between the two free states was modeled through pair-wise exchanges between the 192 spherical diffusion sites corresponding to the same orientation in both states. Simulated decays utilized time points identical to those used in the experiment. QCPMG time domain evolution and $R_{1\rho}$ simulations included the full Liouvillian treatment with 200 crystallites. All simulations were performed in Matlab and utilized selected blocks from the EXPRESS program.(*13*) Best fits for the dynamic parameters of the models were determined by minimization of χ^2 for predictions of the model for ^{2}H QCPMG and $R_{1\rho}$ relaxation rates. The errors were obtained by the inverse covariance matrix method calculated with Monte-Carlo sampling of the model parameters. The errors in the sigmoidal curve parameters (Eq. 1 of the main text) for the temperature dependence of p_{bound} were obtained by the inverse covariance matrix method for the mean-squared errors.

VI. Dark-field TEM MPL data collection

Dark-field images can be obtained using a conventional TEM set-up by tilting the incident electron beam by a small angle so that it is blocked by the objective aperture after it encounters the sample. All the dark-field TEM images for the MPL measurements were collected using an FEI Morgagni microscope at 80 kV with unstained samples, using a side-mounted Advanced Microscopy Techniques Advantage HR CCD camera. The TEM samples were prepared using similar protocols as the regular imaging with uranyl acetate staining. The internal standard tobacco mosaic virus (TMV) solution was co-incubated with the fibril solution during the sample deposition to TEM grids. The dark-field TEM images were taken with 44× and 28× magnifications. Images were analyzed with ImageJ software. Only fibrils that appeared to be single filaments were selected for the MPL measurements. For the extraction of the MPL values, image intensities were integrated over rectangular areas of around 80 nm in length centered on the fibril segments. Rectangular widths were chosen to encompass the fibrils. The resulting intensities are denoted by I_{F} below. The background intensities were taken on both sides of each individual fibril segment and denoted by I_{B1} and I_{B2}. The same procedure was employed for the TMV standard, with the individual intensities denoted as I_{TMV} and backgrounds as I_{B3} and I_{B4}. The value of $\langle I_{TMV} \rangle = \langle I_{TMV} - 1/2(I_{B3} + I_{B4} \rangle$ was calculated as an average of all TMV data under the identical tilt angle of the beam. The known value of MPL for TMV (MPL_{TMV}) is 131 kDa/nm (*14*). The MPL values are given by $MPL = \frac{MPL_{TMV}\,(I_F - 1/2(I_{B1} + I_{B2}))}{\langle I_{TMV} \rangle}$. The resulting MPL values were grouped in bins of 2 kDa/nm for the construction of the histograms. The two-Gaussian fit utilized the minimum distance estimation with the Kolmogorov–Smirnov criterion, which confers increased robustness (*15*).

Figures

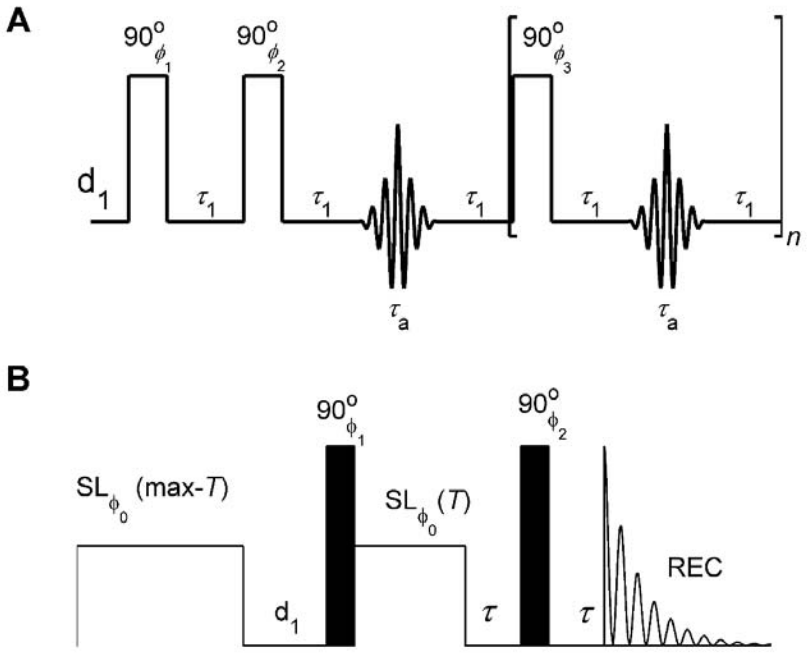

Figure S1. A) The QCPMG pulse sequence for ^{2}H nuclei. Quadrupolar echo block with the 90^o pulses shown as rectangles is followed by a full echo acquisition period (τ_a) and then proceeds to an *n* repeating multiple echo unit (in square brackets). d_1 is the inter-scan delay, and τ_1 is the pulse ringing delay $\tau_{qcpmg} = \tau_a + 2\tau_1 + 90^{\circ}/2$. The analysis of decay curves starts with the first full echo in brackets. The following 16-step phase cycle is used: ϕ_1=*x,y,-x,-y*; ϕ_2= *y,x,y,x,-y,-x,-y,-x*; ϕ_3= *y,x,y,x,-y,-x,-y,-x, -y,-x,-y,-x, y,x,y,x*; ϕ_{rec}= *-x,-y,x,y*. B) Pulse sequence for static ^{2}H solid-state $R_{1\rho}$ measurements. The heat compensation block SL(max-*T*) is followed by the inter-scan delay d_1 and the preparation 90^o pulse, followed by a variable spin-lock delay SL(*T*). The detection is accomplished using the quadrupole echo scheme, $\tau - 90^{o} - \tau$. The phase cycle corresponds to ϕ_0=*x*; ϕ_1= *-y,y*; ϕ_2= *-x,x*; receiver= *-y,y*.

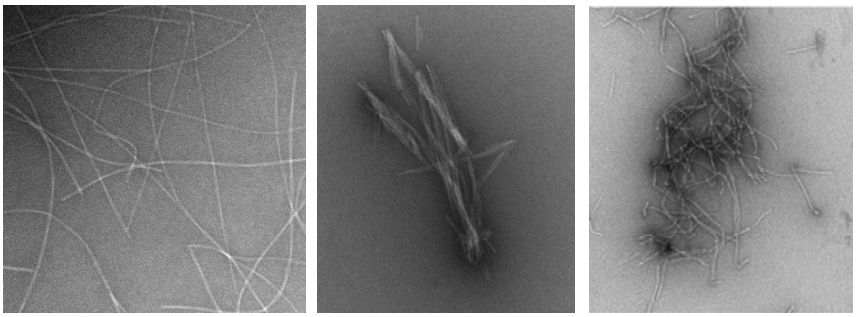

Figure S2. Additional examples of negatively stained TEM images of the mature isoD7 (cross-seeded with the 3-fold wild-type fibrils), ΔE3, and E22Δ $A\beta_{1\text{-}40}$ fibrils.

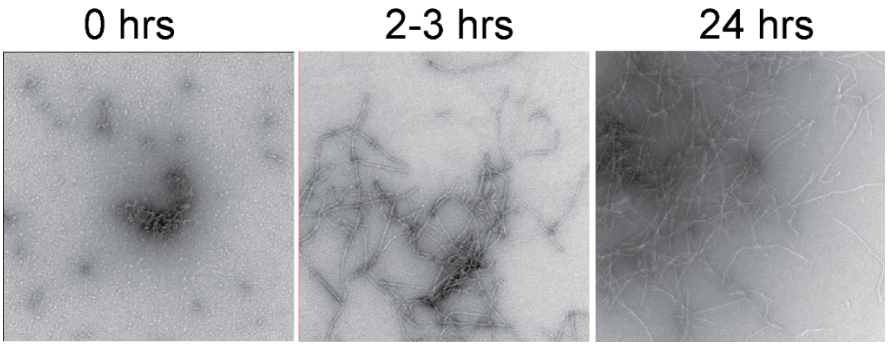

Figure S3. Negatively stained TEM images of the E22Δ $A\beta_{1\text{-}40}$ fibrils at three time point points during the fibril formation process.

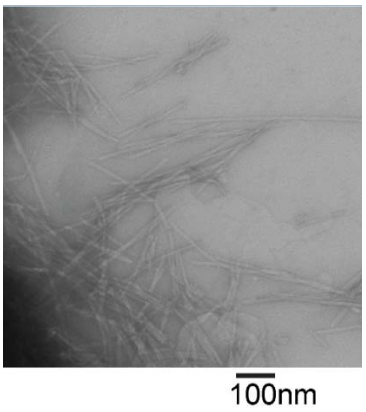

Figure S4. A negatively stained TEM image of the pyroglutamate-3 $A\beta_{1\text{-}40}$ fibrils prepared using the same protocol as the one used for the ΔE3 fibrils.

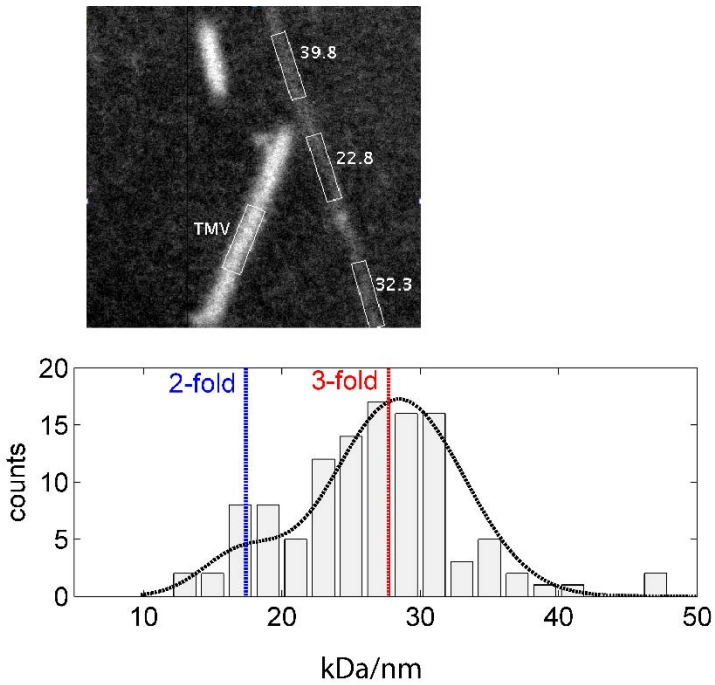

Figure S5. Top panel: Dark-field images of isoD7 amyloid fibrils resulting from the cross-seeding procedure with the wild-type $A\beta_{1\text{-}40}$ in the 3-fold symmetric polymorph. Rectangular areas demonstrate examples of fibril fragments along the long axis chosen for quantitative MPL analysis, with numerical values labeled. Tobacco mosaic virus rods used as standard are labeled "TMV". Bottom panel: Resulting MPL histograms. Vertical dashed lines correspond to the average MPL values of the wild-type 2-fold symmetric polymorph (blue) and 3-fold symmetric polymorph (red), as previously determined by a similar approach (*16*). The fit of MPL data to two Gaussians (dotted black line) are overlaid over the histograms. The fit yielded central values within the ranges for the 3-fold and 2-fold polymorphs with populations of 0.89 and 0.11, with the mean values of 15.9 and 27 kDa/nm, and the widths of half-heights of 6.6 and 11.1 kDa/nm, respectively.

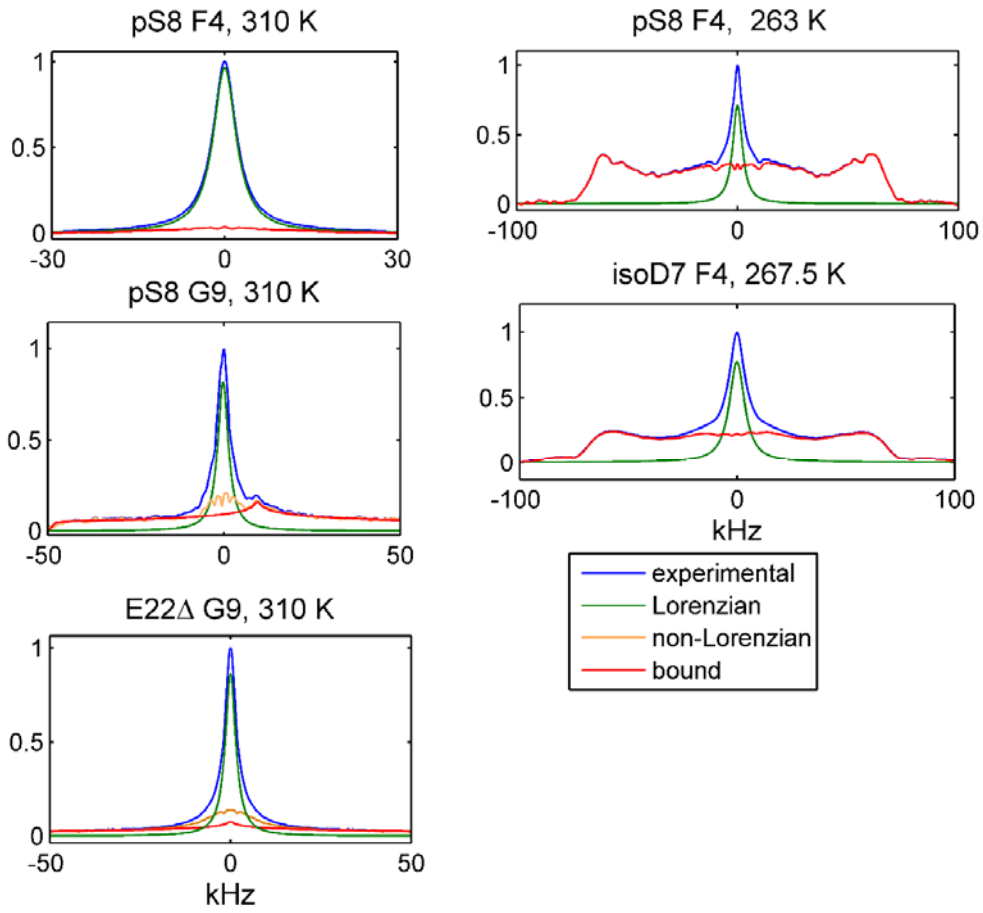

Figure S6. Examples of decomposition of ^{2}H static line shapes into components for determination of the fractions of the bound and free states. For cases in which there is no separate non-Lorentzian line shown, all of the non-Lorenzian component is attributed to the "bound" state.

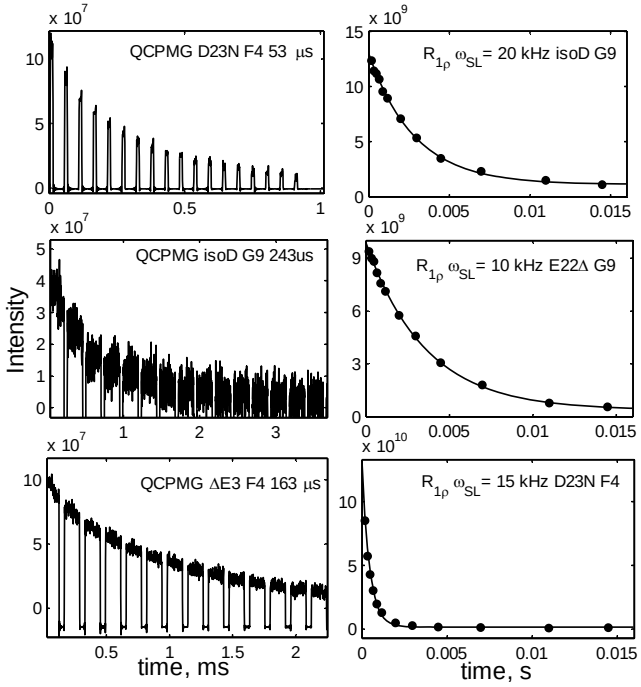

Figure S7. Examples of the experimental magnetization decay curves $M(t)$ obtained from the ^{2}H $R_{1\rho}$ and QCPMG experiments. For the $R_{1\rho}$ experiment, peak intensities are in arbitrary units, obtained via the integration of the central spectral component over the half-height region, versus time (circles). The lines represent the mono-exponential fits of the form $M(t) = Ae^{-t/T_{1\rho}} + B$. For the QCPMG experiment, the examples of the time domain data are shown from the first echo in the loop (designated by the square brackets in the pulse sequence of Figure S5). The type of experiment, variant label, and the values of ω_{SL} or τ_{QCPMG} are shown directly on the graphs.

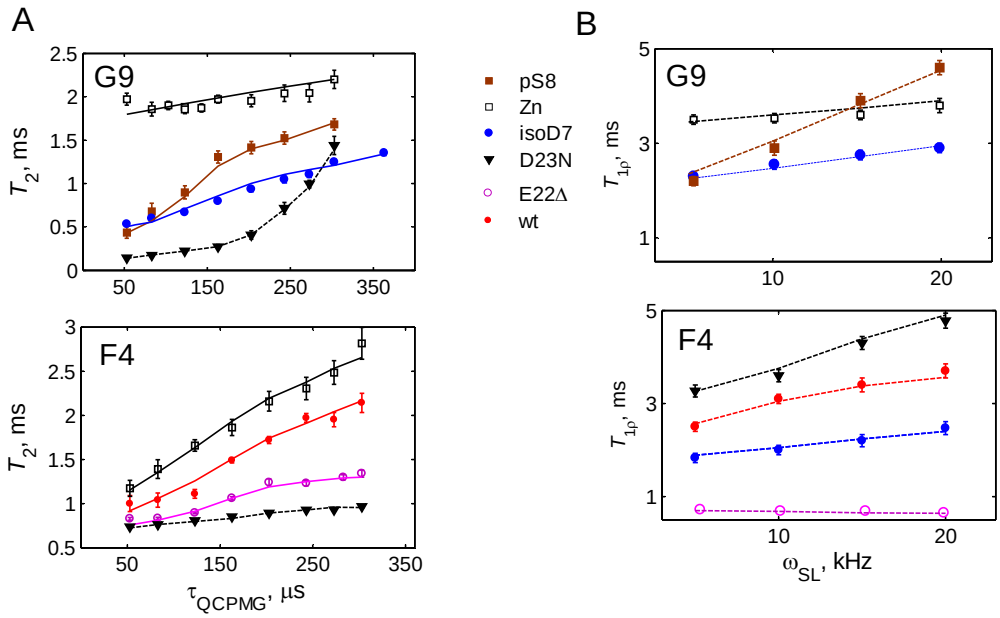

Figure S8. Representative fits of experimental QCPMG rates (A) and ^{2}H $R_{1\rho}$ rates (B). Fits are shown by the lines according to models of Figure 3 of the main text.

References

1. Harris, J. R., and Horne, J. W. (1991) Negative Staining, in Electron Microscopy in Biology (Harris, J. R., Eds.), pp 203-228, Oxford: IRL Press.
2. Dubochet, J., Groom, M., and Mueller-Neuteboom, S. (1082) The mounting of macromolecules for electron microscopy with particular reference to surface phenomena and the treatment of support films by glow discharge., in Adv. Opt. Electron Microsc. (Barrer, R., and Cosslett, V. E., Eds.), pp 107-135.
3. Gor'kov, P. L., Chekmenev, E. Y., Li, C., Cotten, M., Buffy, J. J., Traaseth, N. J., Veglia, G., and Brey, W. W. (2007) Using low-E resonators to reduce RF heating in biological samples for static solid-state NMR up to 900 MHz, J. Magn. Reson. 185, 77-93.
4. Vold, R. L., and Vold, R. R. (1991) Deuterium Relaxation in Molecular Solids, in Advances in Magnetic and Optical Resonance (Warren, W., Ed.), pp 85-171, Acadenic Press, San Diego.
5. Vugmeyster, L., and Ostrovsky, D. (2019) Deuterium Rotating Frame NMR Relaxation Measurements in the Solid State under Static Conditions for Quantification of Dynamics, Chemphyschem. 20, 333-342.
6. Larsen, F. H., Jakobsen, H. J., Ellis, P. D., and Nielsen, N. C. (1998) High-field QCPMG-MAS NMR of half-integer quadrupolar nuclei with large quadrupole couplings, Mol. Phys. 95, 1185-1195.
7. Vugmeyster, L., Au, D. F., Ostrovsky, D., and Fu, R. (2019) Deuteron solid-state NMR relaxation measurements reveal two distinct onformational exchange processes in the disordered N-terminal domain of amyloid-b fibrils, ChemPhysChem. 20, 1680.
8. Au, D. F., Ostrovsky, D., Fu, R., and Vugmeyster, L. (2019) Solid-state NMR reveals a comprehensive view of the dynamics of the flexible, disordered N-terminal domain of amyloid-β fibrils, J. Biol. Chem. 294, 5840–5853.
9. Vega, A. J. (1992) MAS NMR spin locking of half-integer quadrupolar nuclei, J. Magn. Reson. 96, 50-68.
10. van der Maarel, J. R. C. The relaxation dynamics of spin 1=1 nuclei with a static quadrupolar coupling and a radio-frequency field, J Chem Phys 99, 5646-5653.
11. Abragam, A. (1961) Principles of Nuclear Magnetism, Clarendon Press, Oxford.
12. Persson, P.-O., and Strang, G. (2004) A Simple Mesh Generator in MATLAB, SIAM Rev. 46, 329-345.
13. Vold, R. L., and Hoatson, G. L. (2009) Effects of jump dynamics on solid state nuclear magnetic resonance line shapes and spin relaxation times, J. Magn. Reson. 198, 57-72.
14. Namba, K., and Stubbs, G. (1986) Structure of tobacco mosaic virus at 3.6 A resolution: implications for assembly, Science 231, 1401-1406.
15. Parr, W. C., and Schucany, W. R. (1980) Minimum Distance and Robust Estimation, J. Am. Stat. Assoc. 75, 616-624.
16. Chen, B., Thurber, K. R., Shewmaker, F., Wickner, R. B., and Tycko, R. (2009) Measurement of amyloid fibril mass-per-length by tilted-beam transmission electron microscopy, Proc. Natl. Acad. Sci. U.S.A. 106, 14339-14344.